
ELSEVIER
VOLUME 36 ISSUE 3 MARCH 2014 ISSN 13504533
MEDICAL ENGINEERING & PHYSICS
IPEM
Institute of Physics and Engineering in Medicine

Medical Engineering & Physics 36 (2014) 391–396

Contents lists available at ScienceDirect

Medical Engineering & Physics

journal homepage: www.elsevier.com/locate/medengphy

Technical note

Marker-based validation of a biplane fluoroscopy system for quantifying foot kinematics

Joseph M. Iaquinto[a,b], Richard Tsai[a], David R. Haynor[c], Michael J. Fassbind[a], Bruce J. Sangeorzan[a,d], William R. Ledoux[a,b,d,*]

[a] Department of Veterans Affairs, RR&D Center of Excellence for Limb Loss Prevention and Prosthetic Engineering, VA Puget Sound Health Care System, Seattle, WA, United States
[b] Department of Mechanical Engineering, University of Washington, Seattle, WA, United States
[c] Department of Radiology, University of Washington, Seattle, WA, United States
[d] Department of Orthopaedics & Sports Medicine, University of Washington, Seattle, WA, United States

ARTICLE INFO

Article history:
Received 3 February 2013
Received in revised form 31 July 2013
Accepted 27 August 2013

Keywords:
Biplane fluoroscopy
X-ray
Foot
Biomechanics

ABSTRACT

Introduction: Radiostereometric analysis has demonstrated its capacity to track precise motion of the bones within a subject during motion. Existing devices for imaging the body in two planes are often custom built systems; we present here the design and marker-based validation of a system that has been optimized to image the foot during gait.

Methods: Mechanical modifications were made to paired BV Pulsera C-arms (Philips Medical Systems) to allow unfettered gait through the imaging area. Image quality improvements were obtained with high speed cameras and the correction of image distorting artifacts. To assess the system's accuracy, we placed beads at known locations throughout the imaging field, and used post processing software to calculate their apparent locations.

Results: Distortion correction reduced overall RMS error from 6.56 mm to 0.17 mm. When tracking beads in static images a translational accuracy of 0.094 ± 0.081 mm and rotational accuracy of $0.083 \pm 0.068°$ was determined. In dynamic trials simulating speeds seen during walking, accuracy was 0.126 ± 0.122 mm.

Discussion: The accuracies and precisions found are within the reported ranges from other such systems. With the completion of marker-based validation, we look to model-based validation of the foot during gait.

Published by Elsevier Ltd on behalf of IPEM.

1. Introduction

Studying joint kinematics in vivo allows us to quantitatively describe how the load bearing structures within our body move and function during normal use. The ability to quantify bone motions with very small errors, which is necessary to detect subtle but biomechanically significant phenomena, is greatly enhanced by improving the accuracy and precision of the primary measurements. At the same time, due to the importance of subtle motions, it is critical to ensure that the measurement process adds minimal error to joint kinematics.

Optical marker tracking has long been a standard research tool due to its non-invasive nature, flexibility in marker placement, and easy availability of hardware and software. The main limitation of optical systems is that they do not measure bone motion directly. Instead, bone position is estimated from skin-mounted markers, producing an error termed the skin tissue artifact (STA). The STA has been measured by comparing optical marker estimates of motion to direct X-ray imaging of bones in living subjects, finding single marker STA-related errors up to 4.3 mm [1] and grouped marker (cluster) errors ranging from 6.46 to 16.72 mm [2]. STAs of 3–7 mm have been found when compared to bone mounted markers in dynamic cadaver trials [3]. To further complicate the issue, STA varies by marker location, in a unique and unpredictable manner; this was explored in living subjects [4]. X-ray based radiostereometric analysis (RSA) is potentially well suited to measure bone position without STA, thus increasing kinematic accuracy. Additionally, systems using RSA do not burden the subjects with the physical attachment of measurement hardware, which may allow for a more natural gait.

Fluoroscopic systems designed for the precise capture of bone kinematics, unlike optical systems, are not at present commercially available, requiring the creation of the instrumentation in-house.

* Corresponding author at: ms 151, VA Puget Sound, 1660 S. Columbian Way, Seattle, WA 98108, United States. Tel.: +1 (206) 768 5347; fax: +1 (206) 277 3963.
E-mail address: wrledoux@u.washington.edu (W.R. Ledoux).

1350-4533/$ – see front matter. Published by Elsevier Ltd on behalf of IPEM.
http://dx.doi.org/10.1016/j.medengphy.2013.08.013

As these devices are expected to reliably quantify motion on the sub-millimeter scale, several types of system validation are necessary to evaluate their performance. Such validation typically includes: determining the resolution of the hardware imaging chain, evaluating how the hardware and software reduce or eliminate various distortions that are inherent in such systems, and measuring static and dynamic accuracies and precisions based on precisely known positions and motions. Exhaustive validation of these systems along these lines has been previously reported [5–8].

The hardware design, software filtering and pre-processing, and marker-based validation of a new fluoroscopic biplanar system are described in the work presented here. The first and main use for this device will be imaging of the foot, though its flexibility allows for the imaging of any joint of the body.

2. Methods

2.1. X-ray generation

The overall design of our system was modified from a previously developed biplane fluoroscopic system [8,9]. Imaging is performed with a pair of Phillips BV Pulsera fluoroscopic C-arm systems (Philips Medical Systems; Best, The Netherlands). The Pulseras were structurally modified by mechanically disarticulating the X-ray generators and image intensifiers from the "C" of the C-arm, while leaving all the electrical connections in their original configuration. The detached X-ray generator and image intensifier units were then separately mounted on custom designed 5-degree-of-freedom mobile stands, built using 80/20 aluminum framing (80/20 Inc.; Columbia City, IN), that were created specifically to support and balance these components. This mounting methodology requires manual alignment of the X-ray generators and image intensifiers, but it also makes it possible to move these components independently of each other, while allowing the subjects to walk unfettered.

To reduce unnecessary X-ray exposure, the Pulseras' exposure control boards were replaced with synchronized boards, custom built by Philips, that allow a single button press to energize both systems within 80 μs. As a reference point, the estimated full body equivalent dose for a subject performing multiple (30) walking trials through the imaging area is 8 mrem.

2.2. Walkway and imaging area

A custom, hand railed walkway (1 m wide × 6.5 m long) was built using an 80/20 aluminum framework (Fig. 1). The center panel or "imaging area" panel was constructed of a radiolucent composite of thin carbon fiber panels laminated to structural foam (Accuray, ACP Composites Inc.; Livermore, CA). The aluminum frame was designed so that the central imaging panel can be removed for system alignment and distortion correction, as described below. The portion of the frame around the imaging panel allows the mounted image intensifier stands to be rolled underneath to facilitate imaging through the surface of the walkway, making it possible to image obliquely and with significant superior–inferior orientation through the foot.

2.3. Imaging and data collection

The image intensifiers have an approximate 30 cm diameter, with an active area of approximately 27 cm in diameter. The CCD camera that comes with the BV Pulsera has a maximum sampling frequency of 30 Hz, which can be too slow to image all foot bone kinematics during gait without significant loss of information. To improve image acquisition speed, the CCD cameras were replaced with high speed CMOS cameras (Phantom v5.2, Vision Research Inc; Wayne, NJ) that are capable of 1000 Hz grayscale image capture with a 997 μs shutter speed (duration of sensor exposure). The cameras have a resolution of 1152 × 896 pixels, and can collect ∼3 Gb of data (approximately 3 s of data capture at maximum frame rate). The cameras are external to the Phillips imaging chain, and are connected to a separate laboratory computer for data storage. The cameras, and the modified dual fluoroscopes, are triggered simultaneously by a single custom built switch box.

2.4. Alignment

Each time the X-ray generator is moved, it must be aligned such that its beam is both normal to and centered on the image intensifier. Misalignment reduces image contrast and brightness, wastes X-ray exposure and can also create a non-uniform smear in the image and reduce field of view. Alignment is achieved using a guide laser built into each X-ray generator to determine if the source and image intensifier are parallel and centered.

2.5. Distortion correction, bias correction, and localization

These pre-processing algorithms were custom written in Matlab (MathWorks, Natick, MA).

2.5.1. Distortion correction

There are two major sources of distortion in the data collection chain [10], namely pincushion distortion and magnetic lens distortion. To correct for these distortions, a round aluminum plate with laser cut 3 mm diameter holes equally spaced 1.5 cm apart is rigidly fixed to the input side of the image intensifier. A few specifically placed 5 mm holes allow for the automatic detection of the orientation and center of the image intensifier. After being imaged on each fluoroscope, the known size and pattern of the centroids of the holes in the calibration plate are used as control points. The imaged locations of these control points are then used with a thin plate spline algorithm (approximation method) to generate a correction map, which allows us to spatially re-map (correct) every distorted image [11]. The root mean square (RMS) error between the image points and the control points was calculated before and after correction.

2.5.2. Bias correction

The final image quality issue deals with intensity bias which arises from the variation of pixel saturation across an image [10]. As a result, the images captured show a non-uniform brightness which varies in space. The effect of this is that both the beads (and later bones) will vary in their intensity and contrast depending on their location in the image field. Accounting for this bias would increase the consistency of the image characteristics (i.e., contrast and raw intensity values). To correct for this, at every exposure setting (kV and mA) used for data collection or for post processing, a shot is taken with nothing between the X-ray sources and image intensifiers to give an estimate of the intensity distribution in space. The maximum single pixel intensity of this blank image is then subtracted from the whole image to yield a bias map for each image intensifier. This bias map is then applied to every image obtained to normalize the intensity across the image. While considerable image uniformity improvement results from these corrections, in practice they do not create a perfectly uniform background, as the presence and movement of objects in the beam further alters intensity.

2.5.3. Localization

For accurate 3D motion correlation from stereoscopic imaging, the location and orientation of the image intensifiers relative to one another must be precisely known. To obtain this information we created a 3D calibration block from dimensionally

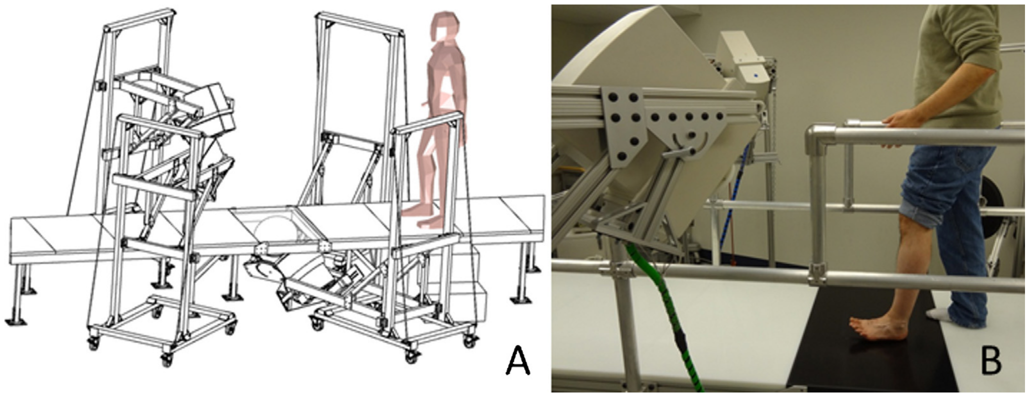

Fig. 1. (A) Biplane imaging path with subject, walkway, X-ray generating and image intensifier mobile stands; (B) subject stepping into the imaging field.

stable plastic (R1/HG3000, GoldenWest MFG., Inc.; Cedar Ridge, CA) with layers of differently sized tantalum beads press fit into it (Fig. 5A). The centroid location and size of these beads were measured to within 0.007 mm using a coordinate measuring machine (CMM, Global Performance model, Hexagon Metrology; North Kingstown, RI). To determine the location of each camera in the global coordinate space, the 3D calibration block is imaged with both fluoroscope systems simultaneously. In order to develop the model of the extrinsic camera parameters, the positions of each bead projection must be calculated on the fluoroscopic images. A threshold algorithm is applied to both fluoroscopic images to identify the beads. The position is then calculated using a weighted intensity centroid. Once this is determined, the beads on the fluoroscope are identified and matched to their 3D bead position. With this correlation, a standard direct linear transformation (DLT) [12] (http://www.kwon3d.com/theory/dlt/dlt.html) matrix can be found using a least squares optimization. From this DLT calculation we obtain extrinsic and intrinsic camera parameters, which are used later to create our virtual imaging environment.

2.6. Line pair and focusing (resolution)

The output illuminations from the image intensifiers are collimated. Using standard radiographic line pair test patterns, for each system we adjusted the focus of the lens on the high speed camera to the sharpest image quality. The radiographic line pair test patterns have calibration marks such that images of these tools denote line thickness resolution, a measure of optical resolution in the biplane system [5].

2.7. Marker-based trials

To validate both the hardware and the pre-processing software, a series of tests were performed using three small (1.6 mm dia.) tantalum beads, which were embedded in another piece of machinable plastic (5 cm by 2 cm by 2 cm); this bead embedded plastic is referred to hereafter as the "wand" (Fig. 2A). The furthest beads within the wand are located 4 cm from each other – on the scale of a foot bone dimension. These beads are readily identified in images as small spheres that are of much higher intensity than background. The location of each bead was known within 0.007 mm (via CMM). In order to determine the system performance, the bead markers were identified on the fluoroscopic images. Using positions of the beads on each fluoroscope and the DLT parameters, a 3D reconstruction of the bead centroids, and thus bead position, can be calculated. This measured position can then be compared to a gold standard allowing for quantification of the system performance.

Using the wand, both static and dynamic marker-based tracking tests were performed. For *static trials*, the wand was mounted to a linear stage; the position of the linear stage was controlled by a high precision stepper motor which could advance the stage in 0.01 mm increments, or in its rotational configuration, rotate with 0.01° increments. For translation: the wand was positioned at 19 different locations on a linear path along the axis of the walkway. Each location represented a linear translation with increments ranging from 0.01 mm to 5 mm. There were 19 locations (18 linear displacements), 3 beads in the wand, and as each position was measured 9 separate times (90 static frames, with groups of 10 consecutive images averaged for noise reduction), for a total of 486 data points. For rotation: the wand was positioned in 16 rotations about a fixed axis, with increments of 0.01°, 0.1°, and 10°. With these 16 positions (5 positions at each increment of motion, 1 zero position), 3 beads, and as each position was again measured from 9 separate frames, a total of 405 data points were collected. Note that two additional beads are in the link connecting the wand to the rotational stage, allowed us to determine the axis of rotation. The whole assembly was supported such that only the wand was visible in the imaging field (Fig. 2B). When performing *dynamic trials*, the wand was fixed to the end of a 1.3 m radio-transparent holder, and manually passed through the imaging field at a velocity of approximately 1 m per second. A total of 960 individual frames (0.96 s of movement at 1000 Hz) were collected. With the three bead locations known (with respect to each other) to within 0.007 mm, accuracy and precision were calculated from the inter-bead distance of beads 1–2, 2–3, and 1–3. This gave 2880 data points. All imaging was performed at the full 1000 Hz sampling rate with kV and mA adjusted for best bead to background contrast (Fig. 2C).

To analyze these data, *accuracy* was defined as the RMS error between the known and measured position of the tantalum beads, while *precision* was defined as the standard deviation of that difference. For the static translation and rotation tests, the "gold standard of measure" was the known movement of the beads relative to their initial position on the linear/rotational stage; for dynamic tests, the "gold standard of measure" was the known CMM bead-to-bead distance.

3. Results

3.1. Distortion correction, bias correction, and localization

3.1.1. Distortion correction

Both pincushion and magnetic distortion are visibly corrected via pre-processing (Fig. 3). The overall RMS error in the uncorrected image averages 21.87 pixels (6.56 mm). With correction, we

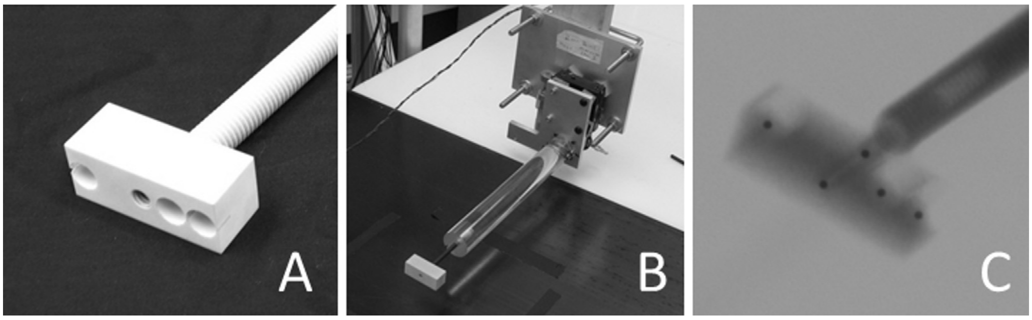

Fig. 2. (A) Plastic wand with beads (inside) and dynamic motion interface (threaded rod); (B) wand fixed to stepper motor/stage in its rotational configuration within the imaging field; (C) fluoroscope image of wand and beads. Note that the two beads near the center of the wand are actually imbedded in the rod linking the wand to the rotational stage. These beads are used to calculate the axis of rotation about which the wand revolves.

can achieve sub-pixel accuracy with an RMS error of 0.51 pixels (0.17 mm).

3.1.2. Bias correction

Applying the bias mapping yields an image with a "flatter" background bias. This can best be appreciated on images of an empty field of view (Fig. 4A and B). The intensity range of an uncorrected "empty" image can be as large as 1300 intensity levels in a 12-bit image, i.e., ~32% of the full range available), whereas the intensity range of a corrected (and empty) image is reduced to near zero (typically less than 5% full range). However, the insertion of an object into the field of view does not permit this correction to be fully realized – the object itself creates a unique background shadow. With a foot in the field of view (Fig. 4C), for example, the intensity range in the image background is approximately 750, or ~18% of the full range available; therefore for this case, the bias correction is only about 44% effective (Fig. 4D).

3.1.3. Localization

Localization determines the geometry of the imaging space, thus a meaningful measure of its accuracy is reflected in the results of the static and dynamic trials (below). With the materials and settings chosen, the pre-processing software is able to automatically distinguish all 15 of the control points (beads) within the 3D calibration block (Fig. 5).

3.2. Resolution

From images of the radiographic line pair test patterns, the system resolution was found to be ~1.6 lines/mm.

3.3. Static and dynamic trials

Static Accuracy and Precision: *Translation* – A translational accuracy of 0.094 mm was found with a translational precision of ±0.081 mm. *Rotation* – A rotational accuracy of 0.083° was found with a precision of ±0.068°. *Dynamic accuracy and precision*: the measured dynamic accuracy was 0.126 mm with a precision of ±0.122 mm.

4. Discussion

This paper has outlined the development and preliminary validation of a custom built biplane fluoroscopy system designed with the intention of overcoming the limitations of traditional retro-reflective motion analysis systems, namely STA. The system has several specific strengths, such as the flexibility in positioning the X-ray generating and detecting components, the ability to allow subjects to walk unfettered through the field of view, and the capability of imaging the foot through a radio-transparent walkway. The modification of the image chain with high speed cameras to collect more rapid changes in bony position with reduced motion blur is an effort to pair the data collection capability of the system with the phenomena it will be employed to study. Slower acquisition rates would probably be adequate for studying the typical motions of other joints.

A series of static and dynamic trials provided a baseline for considering the system's performance both in comparison to existing systems in other labs, and to aid in evaluating the benefit of future upgrades to this system. For static trials, this system's accuracy for translation was 0.094 ± 0.081 mm and for rotation it was 0.083 ± 0.068°. For dynamic trials the system's accuracy

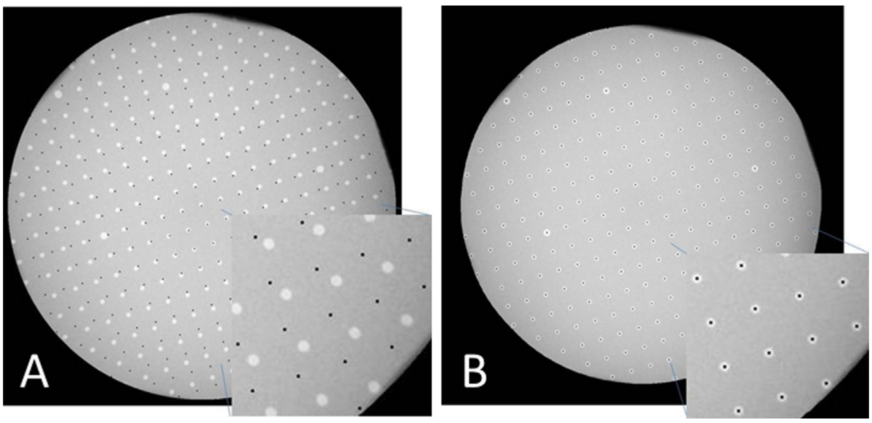

Fig. 3. Fluoroscope image with known control points superimposed. (A) The actual control points (centroid) of each hole are the black dots, and the white circles indicate the distorted holes. (B) Thin plate spline corrected image showing image alignment with the control points.

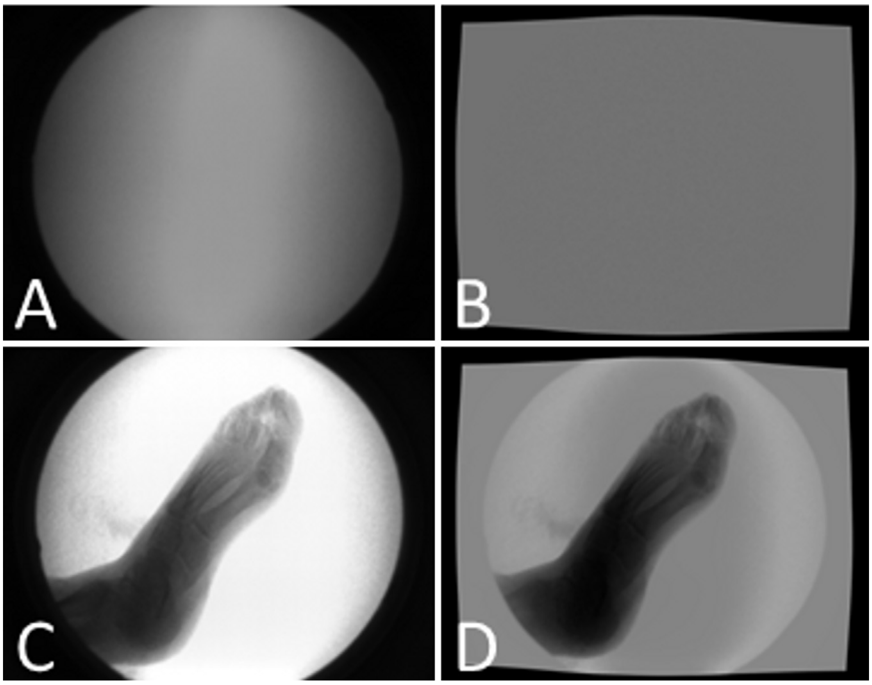

Fig. 4. (A) Fluoroscopic image of an empty field. Note the "cats eye" variation in background intensities; (B) After bias correction has been calculated and applied to the blank image, there is a near perfectly even intensity across the image (border shape change is due to the distortion correction and has no impact on data); (C) phantom foot (XA241L, Phantom Laboratory; Greenwich, NY) prior to image bias correction; (D) phantom foot after bias correction. Note that in this case the background is not perfectly uniform. Also, the phantom foot represents a typical adult sized foot, and in this static image, is completely within the active image area of the system.

was 0.126 ± 0.122 mm. This compares well with the reported performance of other systems in marker-based validation: Tashman and Anderst with a dynamic bias (mean difference between measured and actual) of −0.02 mm when measured with a phantom calibration object, and a in vivo standard deviation of inter-marker distances averaging 0.064 mm [6]; Miranda et al. with static translational and rotational absolute errors of 0.12 ± 0.08 mm and $0.09 \pm 0.08°$, respectively [7]; Brainerd et al. with dynamic "wand" trials yielding a mean absolute error of 0.037 ± 0.046 mm for inter-marker bead distances [5]; Kaptein et al. with static trials that generated an optimized bias of 0.09 mm and precision of 0.03 mm [8]. These studies all sought to quantify the capability of the hardware to detect and measure small but geometrically known and visually distinct objects. The performance of our biplane system, with respect to the image chain and hardware capability, is comparable to that of other current systems – this represents a major step in the validation of our system.

This system has limitations inherent in its specific design. The de-mounted fluoroscope components need to be manually positioned and aligned when imaging with different camera positions. While, with practice, this does not pose a great difficulty, other systems which are built in custom rooms may well offer greater ease and faster alignment when altering camera positions. Additionally, the C-arm units themselves can generate X-rays at a maximum speed of 12.5 pulses per second (or up to 30 pulses per second with additional software), but this is far too slow to capture bone kinematics during gait, necessitating operation in continuous fluoro mode, which has the effect of limiting image capture time and increasing the dosage per study to the patients. Also related to the C-arm units, the image intensifiers have a diameter of only 30 cm, of which slightly less (27) is functional. Because this is comparable to the length of most male feet, it will be challenging to image the hindfoot and forefoot at the same time. Additionally, the need to obliquely image through the floor makes the use of a treadmill (for multiple steps in one exposure)

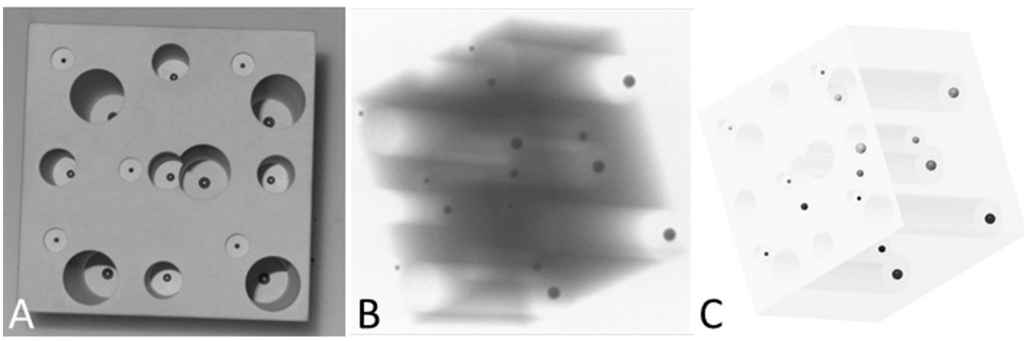

Fig. 5. (A) Plastic 3D localizer block, slanted to show the differently sized beads pressed inside, (B) fluoroscopic image of the block, (C) processed image showing bead location identification for computing the DLT.

difficult, due to the potential introduction of significant image artifacts/beam attenuation from the treadmill hardware.

The primary strengths of the system are its capacity to image through the "ground" and the fact that the subject walks through the image area with a natural, unfettered gait. With the performance of the system's components validated, we are now developing and adding model-based (markerless) tracking capability to the system.

Funding

This research was funded in part by the Department of Veterans Affairs Rehabilitation Research and Development grants A4843C, F7468R and the Magnuson Award. The study sponsor has no role in the study design, in the collection, analysis and interpretation of data; in the writing of the manuscript; and in the decision to submit the manuscript for publication.

Competing interests

None declared.

Ethical approval

Not required.

Acknowledgements

We would like to give special thanks to J. Erik Giphart, PhD and Kevin Shelburne, PhD, for their help in the initial hardware development.

References

[1] Tranberg R, Karlsson D. The relative skin movement of the foot: a 2-D roentgen photogrammetry study. Clin Biomech (Bristol, Avon) 1998;13(1):71–6.
[2] Shultz R, Kedgley AE, Jenkyn TR. Quantifying skin motion artifact error of the hindfoot and forefoot marker clusters with the optical tracking of a multi-segment foot model using single-plane fluoroscopy. Gait Posture 2011;34(1):44–8.
[3] Okita N, Meyers SA, Challis JH, Sharkey NA. An objective evaluation of a segmented foot model. Gait Posture 2009;30(1):27–34.
[4] Nester C, Jones RK, Liu A, Howard D, Lundberg A, Arndt A, et al. Foot kinematics during walking measured using bone and surface mounted markers. J Biomech 2007;40(15):3412–23.
[5] Brainerd EL, Baier DB, Gatesy SM, Hedrick TL, Metzger KA, Gilbert SL, et al. X-ray reconstruction of moving morphology (XROMM): precision, accuracy and applications in comparative biomechanics research. J Exp Zool A Ecol Genet Physiol 2010;313(5):262–79.
[6] Tashman S, Anderst W. In-vivo measurement of dynamic joint motion using high speed biplane radiography and CT: application to canine ACL deficiency. J Biomech Eng 2003;125(2):238–45.
[7] Miranda DL, Schwartz JB, Loomis AC, Brainerd EL, Fleming BC, Crisco JJ. Static and dynamic error of a biplanar videoradiography system using marker-based and markerless tracking techniques. J Biomech Eng 2011;133(12):121002.
[8] Kaptein BL, Shelburne KB, Torry MR, Giphart JE. A comparison of calibration methods for stereo fluoroscopic imaging systems. J Biomech 2011;44(13):2511–5.
[9] Torry MR, Shelburne KB, Peterson DS, Giphart JE, Krong JP, Myers C, et al. Knee kinematic profiles during drop landings: a biplane fluoroscopy study. Med Sci Sports Exerc 2011;43(3):533–41.
[10] Wang JH, Blackburn TJ. The AAPM/RSNA physics tutorial for residents – X-ray image intensifiers for fluoroscopy. Radiographics 2000;20(5):1471–7.
[11] Rohr K, Stiehl HS, Sprengel R, Buzug TM, Weese J, Kuhn MH. Landmark-based elastic registration using approximating thin-plate splines. IEEE Trans Med Imaging 2001;20(6):526–34.
[12] Kwon Y-H. DLT Method; 1998. Available from: http://www.kwon3d.com/theory/dlt/dlt.html